

See discussions, stats, and author profiles for this publication at: <https://www.researchgate.net/publication/280116708>

Conversion of Natural Tannin to Hydrothermal and Graphene-Like Carbons Studied by Wide-Angle X-ray Scattering

ARTICLE in THE JOURNAL OF PHYSICAL CHEMISTRY A · JULY 2015

Impact Factor: 2.69 · DOI: 10.1021/acs.jpca.5b02407 · Source: PubMed

READS

114

8 AUTHORS, INCLUDING:



Katarzyna Balin

University of Silesia in Katowice

21 PUBLICATIONS 54 CITATIONS

SEE PROFILE



J. Szade

University of Silesia in Katowice

132 PUBLICATIONS 821 CITATIONS

SEE PROFILE



Vanessa Fierro

French National Centre for Scientific Research

198 PUBLICATIONS 3,213 CITATIONS

SEE PROFILE



Alain Celzard

University of Lorraine

260 PUBLICATIONS 4,048 CITATIONS

SEE PROFILE

Conversion of Natural Tannin to Hydrothermal and Graphene-Like Carbons Studied by Wide-Angle X-ray Scattering

Karolina Jurkiewicz,^{*,†,‡} Łukasz Hawelek,^{†,‡,§} Katarzyna Balin,^{†,‡} Jacek Szade,^{†,‡} Flavia L. Braghiroli,^{||} Vanessa Fierro,^{||} Alain Celzard,^{||} and Andrzej Burian^{†,‡}

[†]A. Chelkowski Institute of Physics, University of Silesia, ul. Uniwersytecka 4, 40-007 Katowice, Poland

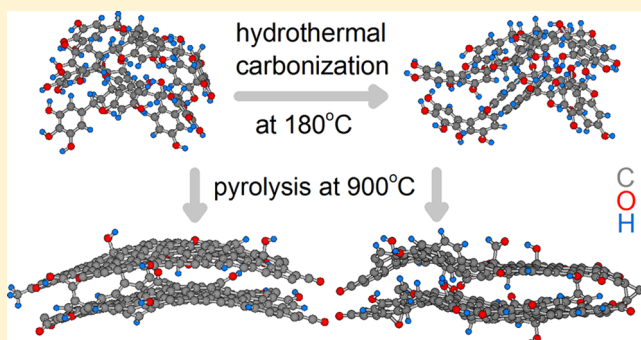
[‡]Silesian Center for Education and Interdisciplinary Research, ul. 75 Pułku Piechoty 1A, 41-500 Chorzów, Poland

[§]Institute of Non-Ferrous Metals, ul. Sowińskiego 5, 44-100 Gliwice, Poland

^{||}Institut Jean Lamour - UMR CNRS - Université de Lorraine n°7198. ENSTIB, 27 rue Philippe Séguin, CS 60036, 88026 Epinal Cedex, France

Supporting Information

ABSTRACT: The atomic structure of carbon materials prepared from natural tannin by two different techniques, high-temperature pyrolysis and low-temperature hydrothermal carbonization, was studied by wide-angle X-ray scattering. The obtained diffraction data were converted to the real space representation in the form of pair distribution functions. The X-ray photoelectron spectroscopy measurements provided information about the chemical state of carbon in tannin-based materials that was used to construct final structural models of the investigated samples. The results of the experimental data in both reciprocal and real spaces were compared with computer simulations based on the PM7 semiempirical quantum chemical method. Using the collected detailed information, structural models of the tannin-based carbons were proposed. The characteristics of the investigated materials at the atomic level were discussed in relation to their preparation method. The rearrangement of the tannin molecular structure and its transformation to graphene-like structure was described. The structure of tannin-based carbons pyrolyzed at 900 °C exhibited coherently scattering domains about 20 Å in size, consisting of two defected atomic layers and resembling a graphene-like arrangement.



INTRODUCTION

For many years, carbon materials have been applied to various domains of life due to their extremely wide range of properties. Nowadays, besides carbon nanomaterials, great attention is given to highly porous carbons. These materials, associated with the advantages of high chemical and thermal stability, lightness, and large surface area and physisorption capacity, have been employed in pollutant adsorption, hydrogen storage, fuel cell electrodes, catalyst supports, and temperature-resistant protection.^{1–4} Porous carbons are produced from organic precursors, including synthetic polymer resins. However, ecological and also cheaper solutions may be found for preparing materials with comparable chemical and physical properties. Among the natural precursors, sucrose, cellulose, and anthracite^{5–7} were successfully used. Recently, new carbons were produced from natural tannin extracts^{8–20} because their properties and price are a really interesting opportunity.¹ Tannin extracts are commercial materials of vegetable origins. Mimosa bark tannin extracts were selected for preparation of carbons investigated in this work due to their easy availability and specific composition. They contain a high proportion of

polyflavonoids (about 80–82%) that present reactive phenolic molecules, so they are able to undergo the same reaction as that of phenol with formaldehyde that is often used as a porous carbon precursor. They are highly porous, cheap, and environment-friendly. Therefore, they can successfully compete with commercial porous carbons.

Porous carbons are usually obtained by controlled pyrolysis of carbonaceous precursors. The pyrolysis under high temperature and flow of inert gas involves decomposition of the starting material. During the process, heteroelements such as oxygen and hydrogen evolve in gaseous form. Simultaneously, free atoms or clusters of atoms of elementary carbon condense into more or less organized layers with a honeycomb lattice. Their atomic arrangement locally tends toward the graphitic structure. However, the process whereby organic materials are transformed into carbon materials is not well understood at the atomic level. The detailed relations between the chemical

Received: March 12, 2015

Revised: June 14, 2015

composition of the precursor, the temperature of heat-treatment, and the atomic arrangement of the resulting carbonaceous materials are still the subject of studies.

The disordered nature of carbons produced by pyrolysis of organic precursors makes the structural characterization a challenge. The first attempt to understand the structure of different pyrolyzed carbons was made by Rosalind Franklin over 60 years ago.²¹ She studied the effect of high temperature treatments on the structure of these materials by X-ray diffraction and made a distinction between graphitizing and nongraphitizing carbons. Nowadays, a number of methods are extensively used for investigating the atomic arrangement of disordered carbons. Transmission electron microscopy offers direct insight into the structure;^{22,23} however, it gives information only from a small volume of the sample and no details concerning the bonds are obtained. The analysis of the chemical composition, types of bonding, and their proportions can be determined by use of electron energy loss spectroscopy²⁴ or X-ray photoelectron spectroscopy (XPS).²⁵ Raman spectroscopy is a method sensitive to short-range atomic ordering and provides information about the degree of disorder and bonding.^{26,27} X-ray and neutron diffraction are methods which provide structural information from a larger volume of a sample. In the case of various carbon materials, detailed information about the atomic arrangement, including the presence of topological defects, can be obtained in the range of the interatomic distances up to about 30 Å.²⁸ Small- and wide-angle X-ray (neutron) scattering patterns allow describing the shape, size, and distribution of pores.^{29,30} The experimental methods can be combined with theoretical calculations such as reverse Monte Carlo, density functional theory, and molecular dynamic modeling,^{31–33} leading to a better understanding of the atomic organization and suggesting structural models.

In the present paper, we propose investigations of the structure of tannin-based materials by the wide-angle X-ray scattering (WAXS) technique. The main purpose of the research is an assessment in the atomic structure transformation of tannin into carbon materials with respect to their preparation method. The effects of the synthesis process and the heat-treatment on the structure of raw tannin were examined on the basis of changes of the X-ray scattering data. The characterization was supported by X-ray photoelectron spectroscopy measurements. As a result of such complementary studies, theoretical three-dimensional models of the atomic structure of the investigated materials were generated using the PM7 (parametric method number 7) semiempirical quantum chemical method.

■ EXPERIMENTAL SECTION

Sample Preparation. Mimosa tannin was used in the form of as-received commercial mimosa bark extract (*Acacia mearnsii*, deWild) kindly supplied by the company SilvaChimica (Italy) under the name Tupafin, and extracted industrially in Tanzania. Such tannin extract is in the form of a light-brown powder, which generally contains 80–82% of actual phenolic flavonoid materials, 4–6% of water, 1% of amino and imino acids, the remainder being carbohydrates. The high proportion of polyflavonoids makes the tannin extract very reactive so it is able to undergo the same reaction as that of phenol with formaldehyde that is often used as a porous carbon precursor.

Hydrothermal carbonization (HTC) was carried out as follows. In a typical experiment, 2 g of tannin were dissolved in 16 g of water and introduced in an open glass vial. The latter

was then placed in a Teflon-lined stainless steel autoclave for HTC. The autoclave was directly installed in a ventilated oven preheated at 180 °C. After 24 h, the autoclave was cooled down to room temperature, and the obtained solid was separated from the remaining aqueous solution by centrifugation and vacuum-dried at 80 °C. More details can be found elsewhere.³⁴

Pyrolysis of both as-received tannin and tannin submitted to HTC was performed in a tubular electric oven, continuously flushed with high-purity nitrogen, heated at 1 °C/min up to 900 °C. The latter set point was maintained for 3 h, after which the resultant carbon was cooled down to room temperature under nitrogen flow.

In the rest of the paper, the investigated samples will be denoted as tannin (natural tannin extract), t-htc180 (natural tannin-based specimen after hydrothermal carbonization at 180 °C), t-c900 (natural tannin extract after standard carbonization at 900 °C), and t-htc180c900 (natural tannin-based specimen after hydrothermal carbonization at 180 °C followed by carbonization at 900 °C).

Measurements. The wide-angle X-ray scattering experiment was performed using a Rigaku-Denki D/MAX RAPID II-R diffractometer equipped with a rotating anode Ag tube ($\lambda_{K\alpha} = 0.5608$ Å), an incident beam (002) graphite monochromator, and an image plate in the Debye–Scherrer geometry as a detector. The investigated samples were ground in a mortar, and the obtained powders were placed inside glass capillaries with a diameter of 1.5 mm and a wall thickness of 0.01 mm. The measurements were carried out at room temperature for the capillaries filled with sample and empty. The diffraction intensity for the empty capillary was then subtracted. The X-ray beam size at the sample was 0.3 mm. All raw two-dimensional diffraction patterns were azimuthally integrated and converted into one-dimensional functions of intensity versus scattering vector Q ($Q = 4\pi \sin \theta / \lambda$, where 2θ is the scattering angle and λ is the wavelength of the incident X-ray beam), up to $Q_{\max} = 22$ Å^{−1}. The intensity functions were corrected for background, polarization, absorption, and incoherent Compton scattering and were normalized using the data processing procedure developed for high energy X-rays.^{35–37} After the data correction, the structure factor $S(Q)$ was computed as

$$S(Q) = \frac{I(Q) - \langle f^2 \rangle - \langle f \rangle^2}{\langle f \rangle^2} \quad (1)$$

where $I(Q)$ is the coherently scattered intensity, normalized to electron units, $\langle f^2 \rangle = \sum_{i=1}^n c_i f_i^2$, $\langle f \rangle = \sum_{i=1}^n c_i f_i$, c_i and f_i are the concentration and the atomic scattering factor of the i th atomic species, respectively, and n is the number of atomic species in the sample. In the next step, the structure factor was converted by the sine Fourier transform to the real space representation of the diffraction data in the form of the pair distribution function (PDF) expressed by the following formula

$$\text{PDF}(r) = \frac{2}{\pi} \int_0^{Q_{\max}} Q[S(Q) - 1] \sin(Qr) \frac{\sin\left(\frac{Q}{Q_{\max}}\right)}{\frac{\pi Q}{Q_{\max}}} dQ \quad (2)$$

where Q_{\max} is the maximum value of scattering vector reached in the measurement, r is the interatomic distance in the real space, and the last term refers to the Lorch damping function that suppresses the undesirable termination ripples from the pair distribution function. The PDF provides information about

spatial correlations between atoms in the investigated sample. The PDF peaks correspond to the distribution of the nearest, second, and next neighbors. The PDF can be regarded as a direct structural probe that is sensitive to local- and intermediate-range order at the nanoscale.

The X-ray photoelectron spectra were acquired with the use of a VGScienta/Prevac spectrometer equipped with an R3000 analyzer. The monochromatized Al $K\alpha$ radiation was used.

COMPUTATIONAL METHODS

The theoretical models of tannin-based structures were optimized using MOPAC 2012 (Molecular Orbital PACKage) with the PM7 semiempirical quantum chemical method developed by Stewart.³⁸ First of all, the models were defined by sets of Cartesian coordinates of the constituent atoms (carbon, oxygen, hydrogen). The atoms in the generated arrangement were not in equilibrium positions. Therefore, the energy of each system had to be minimized to relax the structures. The PM7-implemented MOPAC program was started to solve the Schrödinger equations and to obtain the ground state energy surfaces and the corresponding molecular orbitals. As a result of these simulations, the atoms have been moved to equilibrium positions forming an optimized geometry. In all $S(Q)$ calculations, periodic boundary conditions or super cells were not used. In this case, the computer generated model describes an average coherently scattered domain. The final atomic configurations were used to calculate the theoretical structure factors according to the following equation

$$S(Q) = 1 + \frac{1}{N} \left[\sum_{i=1}^N \sum_{j=1}^N \frac{f_i f_j}{\langle f \rangle^2} \frac{\sin(Qr_{ij})}{Qr_{ij}} \exp\left(-\frac{Q^2 \sigma_{ij}^2}{2}\right) \right]_{i \neq j} \quad (3)$$

where N is the total number of atoms in the model, r_{ij} is the interatomic distance between the i th and j th atoms, the exponential component is the Debye–Waller term incorporating an attenuation of the intensity due to thermal vibrations of atoms, and σ_{ij} is the standard deviation of the interatomic distances. The computed $S(Q)$ function achieves the value of N for $Q = 0$, as can be seen from eq 3. This unwanted small-angle X-ray scattering contribution (or the Debye's volume scattering) was eliminated from the theoretical $S(Q)$ function as described elsewhere.³⁹ The model-based pair distribution functions were computed according to eq 2 from the theoretically calculated structure factors. It is important to point out that the accuracy of the PM7 method in predicted bond lengths for the set of H, C, and O elements is estimated to be 0.019 Å.³⁸ This value was calculated as the average unsigned error in reference sets of atoms of different compounds.

RESULTS AND DISCUSSION

The experimental structure factors $S(Q)$ and pair distribution functions PDF(r) for the investigated materials are shown in Figure 1. Two qualitative conclusions can be drawn from an inspection of the corresponding plots. The tannin and t-htc180 samples exhibit diffraction patterns consisting of broad peaks which are typical for materials with a limited size of coherently scattering regions. The first diffraction peaks appearing at about 1.6 Å^{−1} can be attributed to intermolecular interactions. The first diffraction peak can arise from a variety of structural

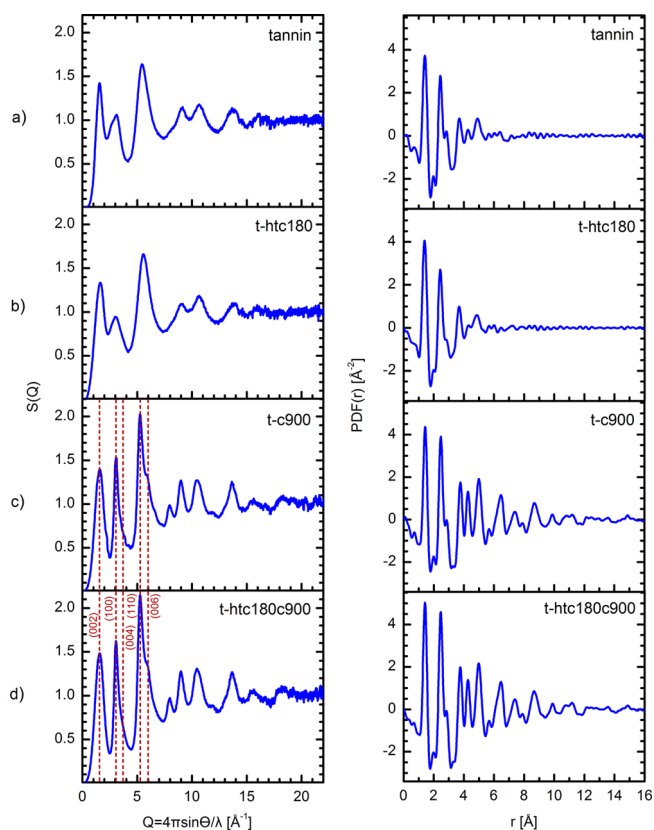


Figure 1. Comparison of the experimental structure factors (left) obtained from wide-angle X-ray scattering of tannin-based materials and pair distribution functions (right) obtained from the structure factor functions.

reasons in noncrystalline materials. In the case of molecular systems, the total measured structure factor can be expressed as the sum of the molecular form factor associated with intramolecular scattering and the molecular packing structure factor describing intermolecular interference. The latter leads to the formation of the first diffraction peak, as was discussed in refs 40 and 41.

The PDFs of the tannin and t-htc180 samples exhibit structure peaks only in a very limited range of the interatomic distances up to about 5.5 Å, as can be seen in Figure 1a,b. In such a range, the PDFs are practically dominated by intramolecular correlations. The first three PDF peaks are related to the intrahexagon carbon–carbon distances. One hexagon is present as a part of the tannin molecule. A slight increase in the amplitudes of the PDF peaks for t-htc180 suggests that the carbonization process began for this sample, even at low temperature.

The considerable changes in the structure factor that can be noticed in Figure 1 c,d, on the left, were led by high temperature pyrolysis of the tannin and t-htc180 samples. The main difference is connected with the shape of the peaks appearing at 3.05 and 5.1 Å^{−1}. They exhibit the right-side asymmetry that is an indication of the turbostratic structure and is typical of a two-dimensional character of the diffraction pattern coming from a single graphitic layer. Such a feature is called “the Warren profile”.^{42,43} On the contrary, no such behavior is observed for the tannin and t-htc180 samples. Moreover, the peaks observed at about 3.1 Å^{−1} for tannin and t-htc180 have clearly lower amplitudes. The peaks seen at about

7.95 Å⁻¹ for the t-c900 and t-htc180c900 samples are not present for tannin and t-htc180. These differences cannot be explained by a simple reduction of a size of coherently scattered domains and additional disorder.

The diffraction peaks for the t-c900 and t-htc180c900 are indeed sharper than those for the tannin and t-htc180 samples and can be assigned to the structures intermediate between crystalline and amorphous. The presented structure factors for the pyrolyzed samples contain only the (00 2*l*) and (*h**k*0) graphitic type reflections. The absence of the general (*hkl*) diffraction peaks indicates the lack of graphitic -ABAB- stacking structure. Such a diffraction pattern is typical of a turbostratic structure characterized by a lack of spatial correlations between individual graphitic layers in the direction perpendicular to them, due to their translation and rotation.⁴⁴ Information about the arrangement of carbon atoms within a single layer can be obtained from (*hkl*) peaks having zero *l* values. A common feature of the structure factor for these samples is the presence of the first diffraction peak (the (002) peak in graphite) occurring at about 1.6 Å⁻¹. The intensity of this peak depends on the number of turbostratically stacked layers in coherent scattering domains of carbon materials.⁴⁵ Its presence indicates that at least two graphitic layers stacked in the structure.

The difference between structural order of tannin-based materials before and after pyrolysis at 900 °C is also clearly seen from the comparison of the PDFs (Figure 1, on the right) obtained through eq 2. The more structured diffraction patterns for the t-c900 and t-htc180c900 samples lead to PDFs which exhibit peaks up to 16 Å. Such behavior can be explained by ordering of the atomic structure and increase in the size of the coherent scattering domains. The amplitudes of the PDF peaks are related to the number of neighboring atoms in the subsequent coordination spheres. Studying the changes in the intensity of these peaks, the evolution of the structure of tannin-based materials can be observed. The lowest amplitudes of the PDF peaks arise for the natural tannin extract sample. As the temperature of heat-treatment of tannin increases, quite different behavior of the experimental PDF can be observed. For the sample subjected to the hydrothermal process at 180 °C, only low variations in the PDF amplitudes occur, but it can be clearly seen that materials after carbonization at 900 °C show a higher degree of ordering within the first and next coordination spheres. The total PDF can be approximated by the linear combination of the partial PDF_{*ij*} as follows

$$\text{PDF}(r) = \sum_{i=1}^n \sum_{j=1}^n \frac{c_i c_j Z_i Z_j}{\langle Z \rangle^2} \text{PDF}_{ij}(r) \quad (4)$$

where $Z_i = f_i(0)$ indicates the atomic number of *i*th atomic kind and $\langle Z \rangle = \sum_{i=1}^N c_i Z_i$.⁴⁶ In the samples heated at higher temperature, the proportion of carbon atoms coordinated by three carbons increases in comparison with the tannin and t-htc180 samples. As the weight of the C–C pairs to the total PDF(*r*) is higher than those of the C–H and O–H pairs, the higher proportion of the C–C bonds can explain observed evolution of the experimental data.

XPS C 1s spectra of t-c900 and t-htc180c900 samples were analyzed in order to specify possible chemical states of the carbon atoms, and identify the oxygen- and hydrogen-containing functional groups. Moreover, the XPS technique can provide useful information on the presence of structural defects. The obtained XPS data for both tannin-based samples after high-temperature carbonization (Figure 2) show that the

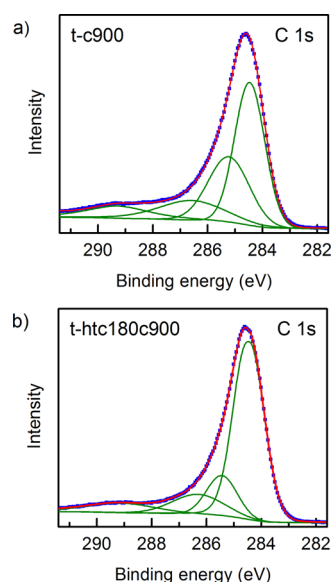


Figure 2. XPS C 1s spectra with deconvoluted peaks for tannin-based sample after standard carbonization at 900 °C (a) and sample after hydrothermal carbonization at 180 °C and standard carbonization at 900 °C (b).

main contribution to the C 1s band is the asymmetric line of graphite type. The line is due to C–C bonds in the hexagonal lattice and is situated at about 284.5 eV, in agreement with the previous photoemission studies of carbon materials.^{47–49} However, one has to remember that carbon atoms bonded to hydrogen have a similar binding energy of about 284 eV. Therefore, some part of the main peak content can be attributed to C–H bonding. For both investigated samples, the second dominant contribution of the C 1s band is observed at about 285.3 eV. This peak can be attributed to the defects of C atom positions within the graphite-like planes. Similar assignment of that contribution in carbon materials was discussed by Datsyuk⁴⁸ or Estrade-Szwarczkopf.⁵⁰

The region at 286–289 eV in the C 1s band corresponds to carbon atoms attached to different oxygen-containing groups. The chemical shifts of about +1.5, +2.5, and +4.5 eV from the main graphitic line are typically assigned to C–OH, C=O, and O=C–OH functional groups, respectively.^{47–50} Around 286 eV, C–O–C epoxide and ether linkages should also be taken into account.⁴⁹ The C 1s spectrum for t-c900 consists of two peaks in the energy range of carbon–oxygen bondings. The first peak at 286.6 eV indicates the presence of single C–O bonds. The position of the second peak at 289.2 eV can be clearly associated with double carbon–oxygen bonds coming from C=O or O=C–OH groups or a mixture of them. From the analysis of the C 1s data of the t-htc180c900 sample, it can be concluded that both C–O and C=O types of bonding are present in the material, as in the case of t-c900. The ratio of single carbon–oxygen bonds to double carbon–oxygen bonds was calculated as the ratio of the peak area at about 286.5 eV to the peak area at about 289 eV. For t-c900 and t-htc180c900 samples, the ratio is 1.5 and 1.4, respectively. As the intramolecular structure of the tannin and t-htc180 samples has been described in refs 8, 9, 51, and 52 providing information about the chemical state of the constituent atoms, their XPS spectra are not shown here.

Taking into account the obtained X-ray diffraction data and earlier studies of the tannin extract by MALDI-TOF mass

spectrometry,^{51,52} the model of the atomic structure of investigated raw, natural, tannin was optimized. We considered the mostly repeating structural fragments characterized by the mass spectroscopy and created the atomic arrangements consisting of the building units linked to each other. The basal structural unit, shown in Figure 3a, is composed of carbon

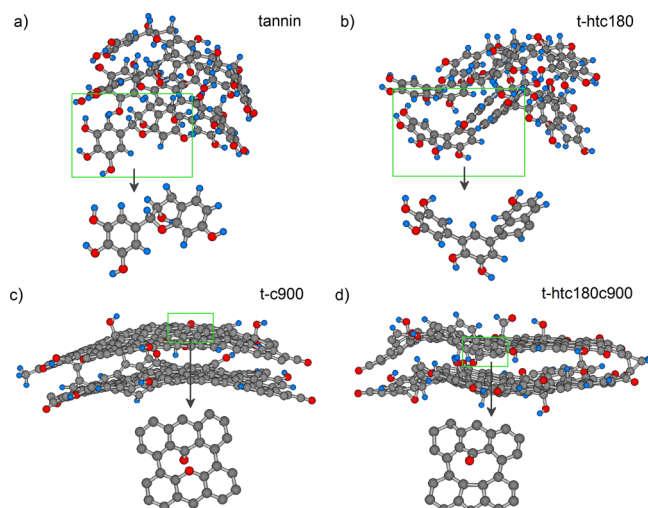


Figure 3. View of the optimized models for the average coherent domains in tannin-based materials (a–d). Carbon atoms are marked in gray, hydrogen atoms in blue, and oxygen atoms in red. The zoom in part a shows the basal structural unit of the natural tannin sample; that in part b shows the fragment of the structural model of tannin after hydrothermal carbonization; and those in parts c and d show the fragment of pyrolyzed carbon structure containing defects.

aromatic hexagons with bonded hydroxyl –OH groups and heterocyclic carbon rings with built-in oxygen atom. Six structural units were connected, and then, the energy of the resultant geometry was minimized by the PM7 semiempirical method. For the relaxed sets of the Cartesian coordinates, the interatomic distances were calculated and then the theoretical structure factors (eq 3) were determined. Subsequently, the theoretical PDFs were computed from the $S(Q)$ (eq 2). The simulated model was chosen so as to reproduce the features of the experimental diffraction data in both reciprocal and real spaces. The amplitude of the first $S(Q)$ peak was correctly reproduced assuming the presence of six tannin molecules in the constructed model, according to suggestions presented in refs 40 and 41 for molecular systems, as has been discussed above. It is important to note that the layered structure is not necessary to explain the formation of the first diffraction peak.

For the quantitative comparison of the tested models, the discrepancy factor R was introduced

$$R = \sqrt{\frac{\sum_i (\text{PDF}_i^{\text{exp}} - \text{PDF}_i^{\text{sim}})^2}{\sum_i (\text{PDF}_i^{\text{exp}})^2}} \quad (5)$$

where $\text{PDF}_i^{\text{exp}}$ and $\text{PDF}_i^{\text{sim}}$ are values of experimental and simulated PDF in each computed point, respectively. The results of the $S(Q)$ and PDF best fits are compared with the experimental data in Figure 4a. The values of the mean deviations of atoms from their equilibrium positions for the generated model were set as 0.055, 0.18, and 0.5 Å for carbon, oxygen, and hydrogen, respectively. The discrepancy factor is 27.9%. From the comparison of the simulation with the

experimental data, it can be seen that the diffraction pattern is relatively well reconstructed. The positions and amplitudes of the PDF peaks are in good agreement to about 5 Å. However, slight discrepancies in the peak positions and amplitudes of $S(Q)$ and PDF can be seen. It should be kept in mind, however, that the investigated raw tannin extract is a natural material of vegetable origin and may thus have a nonhomogeneous structure. Moreover, the diffraction method provides only averaged information about the arrangement of the atoms which form the model. Therefore, it can be concluded that simulated models should be regarded as average and simplified representations of the real structure. The visualization of the proposed atomic model for the tannin material is displayed in Figure 3a.

For further structural characterization of the investigated materials, an attempt has been made to build up the model of structure for tannin treated by HTC. The thermal treatment of water mixed with organic substances such as cellulose or furfural at temperatures up to 300 °C has generated increasing interest in the recent years for producing carbon materials. One of the advantages of the HTC process is the emission of very little gaseous products like CO_2 . In the literature,^{53–55} it is described that hydrothermal carbonization of organic precursors provides carbon materials with a high concentration of oxygen and hydrogen in the form of functional groups such as carbonyls and hydroxyls. From an inspection of Figure 1b, it is observed that, when tannin is hydrothermally treated at 180 °C, the resulting material exhibits an XRD pattern similar to that of pristine tannin, indicating that the atomic structure of the tannin has been preserved. The first PDF peak exhibits a slightly higher intensity for t-htc180 than for tannin. Therefore, one additional carbon hexagon was connected to each tannin molecule. Such a new arrangement allowed finding an optimal configuration of atoms (Figure 3b) that satisfactorily reproduced the experimental $S(Q)$ and PDF (Figure 4b). The presence of an additional hexagonal ring increases the number of intrahexagonal nearest-neighbor carbon–carbon distances. The values of the mean deviations of the atoms from their equilibrium positions were set at 0.05, 0.18, and 0.5 Å for C, O, and H, respectively. The calculated discrepancy factor is 21.8%. Referring to the results of the WAXS experimental data and to the computer simulations, it can be concluded that the structure of natural tannin did not sustain notable changes after hydrothermal carbonization. Indeed, only a slight increase of carbon content, from 53.8 to 59.7 wt %, was reported recently.³⁴ However, the arrangement of the hexagonal carbon rings in the t-htc180 sample can be regarded as the origin of the graphitic structure formation.

In the next step, structure modeling of tannin-based materials pyrolyzed at 900 °C was initiated. Wide-angle X-ray scattering data show that tannin and hydrothermally treated tannin submitted to high-temperature carbonization exhibit characteristics that vary significantly from those of starting materials (Figure 1c,d). In both cases, the structural models are built from hexagons as basic structural units and such an atomic arrangement is typical for graphene-like structure. Similar behavior was earlier noticed by us in a series of activated anthracites.⁵⁶ Our previous paper³¹ has also led to a better understanding of the structure of nanographene platelets, and these results can be compared with the present data indicating resemblance to graphene-like ordering. Due to notable changes in XRD results for samples after high-temperature pyrolysis, a slightly different approach for structure modeling was used. For

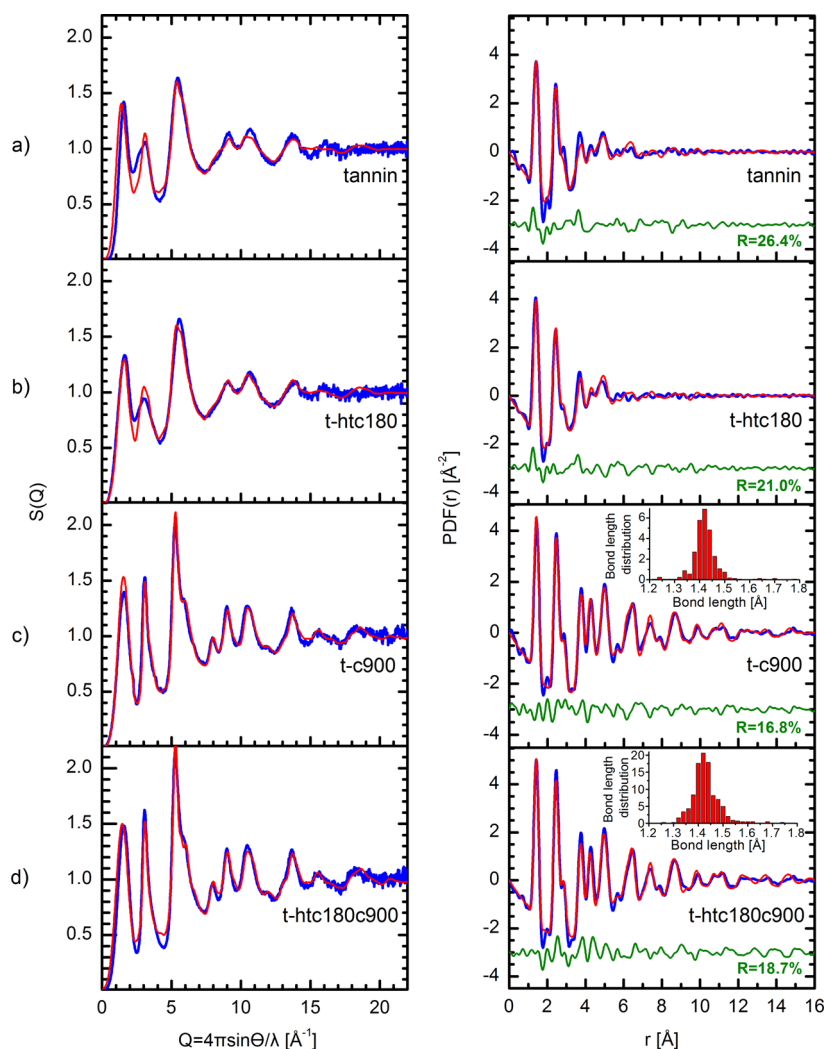


Figure 4. Comparison of the experimental structure factors (left) and the pair distribution functions (right) with the simulation results for models of tannin-based materials (a–d). The experimental data are marked in blue, the simulated data in red, and the difference between them in green. R means the discrepancy factor. The insets of histograms show the C–C bond length distribution.

the correct reconstruction of the experimental $S(Q)$ and PDF features, some aspects had to be considered during the geometry design. The selection of the proper size of the ordered region, and therefore the number of carbon hexagonal rings and their arrangement in each layer, has a significant influence both on the amplitudes and on the range of $S(Q)$ and PDF oscillations. The high temperature applied during the pyrolysis process causes the evolution of volatile chemicals from the starting material. Predominantly, heteroelements are eliminated. However, it is always very difficult to completely avoid the presence of remaining noncarbon atoms during a heat-treatment, even under a protective gas atmosphere and at high temperature. Thus, the local arrangement of carbon atoms can be affected by the presence of heteroelements. In this case, besides C atoms, O and H elements are present in the natural tannin and their occurrence in the pyrolyzed materials can be expected. The starting chemical structure of tannin contains hydroxyl –OH and ether C–O–C groups, as shown in Figure 3a. Hydroxyl groups are relatively easy to remove during heat-treatment; however, those located on the defective sites and edges are hard to remove⁵⁷ and their presence was noticed on the basis of experimental studies and theoretical predictions in a

number of carbon materials after annealing up to about 1000 °C.^{47,58–60}

The stability and evolution of different functional groups during the reduction process on the perfect and defective carbon structures are discussed mainly based on theoretical studies. Due to limitations of experimental techniques, it is rather possible to understand only a qualitative analysis of the surface chemistry. The theoretical considerations^{57,60–62} led to the conclusion that the adsorption of hydroxyl and other functional groups on defective sites and edges of carbon materials is much stronger than that at carbon domains without lattice defects. The interactions of the functional groups at defects are much stronger than those at the pristine lattice, and a higher energy is needed for removing them from the defective sites than from perfect systems. Moreover, it was demonstrated by Kumar et al.⁶³ that stable carbonyl groups in reduced graphene oxide can be favorably transformed to hydroxyl groups at room temperature via carbonyl-to-hydroxyl reaction near carbon vacancies and holes.

The presence of ether groups is taken into account in proposed models of graphene oxide (GO) and reduced graphene oxide (rGO) according to the most recent studies.^{58–60,64} Moreover, the thermal reduction of oxygen-

containing functional groups can lead to the formation of C—O—C ether as well as C=O carbonyl linkages.⁶⁰ Besides, C—O—C epoxy, —COOH carboxyl, and C—H groups were frequently reported in structural analysis of carbon materials.^{59,60,64} In general, there is a wide variability in the type and coverage of the functional groups on carbon materials, primarily arising from differences in preparation and heat-treatment processes. The convergence between the experimental and theoretical PDF depends on the kind and amount of incorporated functional groups. Keeping the ratio of C—O to C=O bonds, obtained from XPS results, and taking into account previous considerations on the possible chemistry of heat-treated carbon materials containing O and H elements, we proposed structural models of the investigated tannin-based carbons.

Some kinds of deviation from the perfect hexagonal lattice in tannin-based carbons, suggested by the presence of a defect peak in the XPS spectra, can originate from the presence of topological defects. In-plane symmetry breaks can include point defects, such as vacancies or Stone–Thrower–Wales defects. They lead to the formation of nonhexagonal rings. Such kinds of imperfections were observed so far in many carbon materials.^{65–67} The appearance of point defects leads to lattice distortions not only in a region close to the defects but also in further surroundings. It is worth mentioning that the curvature of graphene layers caused by the introduction of defects is one of the ideas proposed to understand the formation of porosity in nongraphitizing carbons.⁶⁸

Taking into account the above considerations, the three-dimensional models of tannin-based pyrolyzed carbon structure were constructed and optimized by the PM7 algorithm. The basic structure unit of the starting configuration of the models consists of two graphene sheets containing a total of about 375 carbon atoms. The model size is about 20.5 Å in length and 17.5 Å in width within a single layer. The number of carbon hexagons and their arrangement in each layer of the considered models were chosen to correctly reproduce the amplitudes and the range of $S(Q)$ and PDF oscillations. Oxygen and hydrogen atoms were bonded to carbon atoms, taking into account their possible configurations determined by the XPS data. The mean deviations of the atoms from their equilibrium positions in the proposed model for t-c900 carbon were 0.047, 0.2, and 0.5 Å for the C, O, and H atoms, respectively. The values of the same model parameters for the t-htc180c900 sample were set as 0.035 Å for carbon, 0.15 Å for oxygen, and 0.5 Å for hydrogen. The lower values of these parameters for the t-htc180c900 model indicate that this t-htc180c900 sample is subjected to a higher degree of ordering that can be observed in Figure 1d, where the experimental XRD data exhibit a higher intensity of the peaks. Attempts made to reproduce all the features of the experimental $S(Q)$ and PDFs by models in which the presence of a perfect hexagonal arrangement of the carbon atoms was assumed have proved ineffective. In particular, the $S(Q)$ and PDF peaks were not sufficiently suppressed, which prompted us to impose additional disorder to the constructed models. Therefore, topological defects in the form of monovacancies were introduced and randomly distributed over the graphene network. In both models, three monovacancies per a single layer were introduced. The kind of defects and their concentrations were adjusted to obtain the best agreement with the experimental data. The missing lattice atoms caused a deviation from the ideal hexagonal network and led to the formation of five- and nine-membered rings. Such a situation

leads to the local curvature of the surface and increases the intrinsic disorder. The possible defects creation mechanism in the graphene basal plane was discussed in detail by Bagri et al.^{60,69} In the process of leaving the sheet during reduction by heat-treatment, the oxygen-containing functional groups can create defect sites. Bagri et al. interfered that epoxy and hydroxyl groups present in graphene oxide contribute to the formation of vacancies. The creation of holes leads to breaking C—C bonds, and the valence of the C atoms can be compensated by attaching functional groups. It was shown⁶⁹ using atomic-scale simulations that carbonyl C=O bonds and ether C—O—C rings, which are thermodynamically stable, are favorable. We took into account the theoretical predictions during construction of our structural models of carbonized tannins and included the carbonyl and ether groups on the defect sites (Figure 3c,d). The Cartesian coordinates of atoms for the generated models are listed in the [Supporting Information](#) which can be used to reproduce the simulations presented in our paper.

The carbon–carbon bond length distributions for the models of carbonized tannins are shown in the insets in Figure 4c,d. From an inspection of these plots, it can be seen that the presence of nonhexagonal carbon rings and of oxygen and hydrogen atoms leads to a broader distribution of the nearest-neighbor carbon–carbon bond lengths. Such a kind of broadening can be related to static disorder that extends beyond the defect regions. In the model energy optimization procedure using the PM7 semiempirical method, static disorder due to the presence of the topological defects and noncarbon atomic species leading to the distortion of the whole network is automatically included in the models. The bond lengths shorter and longer than the C—C interatomic distance 1.42 Å, typical for the graphitic structure, can be attributed to the double and single carbon–carbon bond, respectively. These bonds randomly distributed over the whole model are responsible for static disorder present in the final atomic configuration that combines with thermal disorder. The discrepancy factors for the constructed models of t-c900 and t-htc180c900 with monovacancies are 16.8 and 18.7%, respectively. In Figure 3c,d, the final atomic configurations after optimization of the models are displayed. Both models exhibit similar structural features. They consist of two slightly curved carbon layers disordered by defects and noncarbon atoms. Overall, they resemble the structure of defective graphene.

CONCLUSIONS

The present results have demonstrated the conversion of natural tannin into disordered graphene-like structure caused by the pyrolysis process. Analysis of the WAXS experimental data in real and reciprocal spaces by comparison to computer simulations and XPS results allowed the extraction of precise details of the structure of tannin-based materials, such as their coherent domain size, the number of individual layers, and the nature of the disorder. For the tannin and t-htc180 samples, the ordering range is about 5.5 Å and the intramolecular structure of both materials is defined by covalent interaction between C, O, and H constituent atoms. Intermolecular interactions are mainly of the van der Waals type and lead to the molecular arrangement that exhibits the highly disordered structure without crystal-like long-range ordering.

Moreover, it was shown that the present conditions of hydrothermal carbonization were able to yield the material with an atomic arrangement that differs only slightly from the

structure of pristine tannin. A general conclusion can be drawn from the analysis of the tannin structure evolution during processing. Both pristine and hydrothermally treated tannin, which exhibit a highly disordered structure, lose the disorder effectively under an inert atmosphere and at higher temperatures. In the case of t-c900 and t-htc180c900, the size of the coherently scattered domains within a single graphene layer increases to approximately $20.5 \text{ \AA} \times 17.5 \text{ \AA}$. The models which reconstruct correctly the experimental data in both reciprocal and real space contain about 375 atoms arranged within two layers. Six monovacancies, three per a single layer, randomly distributed over the structures were necessary to obtain a very good agreement with the experimental data. These topological defects together with bonding between carbon, oxygen, and hydrogen atoms lead to distortion of the whole in-layer network and curvature of the individual graphene layers. All details of the constructed models can also be perceived from analysis of the atomic coordinates listed in the [Supporting Information](#).

The tannin-based carbons described in the present work are one of a possible series of lightweight carbonaceous materials derived from natural resources. The intrinsic characteristics and physical properties make it an attractive material for use as a low-cost, highly porous, and conducting structural component. It is important to point out that the tannin-based carbons can be derived from renewable and less expensive resources. Interesting properties of these carbons include low-cost precursors, easy batch production and formability at the industrial level, good electrical conductivity, low thermal conductivity, moderate permeability, good mechanical strength, anisotropy, machinability, and fire resistance without formation of hazardous fumes when heated.

As these materials are important from the point of view of their applications and their physical and chemical properties are strongly influenced by the presence of defects, detailed knowledge of the atomic scale structure is necessary for deeper understanding of preparation procedures. Obtained results can be used to improve technological methods of their production. Moreover, as the WAXS method can be considered as a global probe of the structure that provides information about a larger sample volume, the proposed approach is expected to be useful in the characterization of carbon materials and their defect structure when produced on a mass scale for a wide variety of industrial applications.

■ ASSOCIATED CONTENT

● Supporting Information

The Cartesian coordinates of atoms for the generated structural models of tannin-based materials are provided. The Supporting Information is available free of charge on the [ACS Publications website](#) at DOI: [10.1021/acs.jpca.5b02407](https://doi.org/10.1021/acs.jpca.5b02407).

■ AUTHOR INFORMATION

Corresponding Author

*E-mail: kjurkiewicz@us.edu.pl.

Notes

The authors declare no competing financial interest.

■ ACKNOWLEDGMENTS

K.J. acknowledges the support by the FORSZT project cofinanced by EU from the European Social Fund. The French authors gratefully acknowledge the financial support of the

CPER 2007-2013 "Structuration du Pôle de Compétitivité Fibres Grand'Est" (Competitiveness Fibre Cluster), through local (Conseil Général des Vosges), regional (Région Lorraine), national (DRRT and FNADT), and European (FEDER) funds.

■ REFERENCES

- (1) Rodriguez-Reinoso, F. The Role of Carbon Materials in Heterogeneous Catalysis. *Carbon* **1998**, *36*, 159–175.
- (2) Frackowiak, E.; Beguin, F. Carbon Materials for the Electrochemical Storage of Energy in Capacitors. *Carbon* **2001**, *39*, 937–950.
- (3) Mesalhy, O.; Lafdi, K.; Elgafy, A. Carbon Foam Matrices Saturated with PCM for Thermal Protection Purposes. *Carbon* **2006**, *44*, 2080–2088.
- (4) Reed, M. W.; Brodd, R. J. Porous Carbon for Fuel Cell Electrodes. *Carbon* **1965**, *3*, 241–246.
- (5) Wei, L.; Yushin, G. Electrical Double Layer Capacitors With Activated Sucrose-Derived Carbon Electrodes. *Carbon* **2011**, *49*, 4830–4838.
- (6) Lyubchik, S. B.; Benoit, R.; Beguin, F. Influence of Chemical Modification of Anthracite on the Porosity of the Resulting Activated Carbons. *Carbon* **2002**, *40*, 1287–1294.
- (7) Phan, N. H.; Rio, S.; Faur, C.; Le Coq, L.; Le Cloirec, P.; Nguyen, T. H. Production of Fibrous Activated Carbons from Natural Cellulose (Jute, Coconut) Fibers for Water Treatment Applications. *Carbon* **2006**, *44*, 2569–2577.
- (8) Tondi, G.; Fierro, V.; Pizzi, A.; Celzard, A. Tannin-Based Carbon Foams. *Carbon* **2009**, *47*, 1480–1492.
- (9) Zhao, W.; Fierro, V.; Pizzi, A.; Celzard, A. Bimodal Cellular Activated Carbons Derived from Tannins. *J. Mater. Sci.* **2010**, *45*, 5778–5785.
- (10) Szczurek, A.; Amaral-Labat, G.; Fierro, V.; Pizzi, A.; Masson, E.; Celzard, A. The Use of Tannin to Prepare Carbon Gels. Part I: Carbon Aerogels. *Carbon* **2011**, *49*, 2773–2784.
- (11) Szczurek, A.; Amaral-Labat, G.; Fierro, V.; Pizzi, A.; Celzard, A. The Use of Tannin to Prepare Carbon Gels. Part II. Carbon Cryogels. *Carbon* **2011**, *49*, 2785–2794.
- (12) Amaral-Labat, G.; Szczurek, A.; Fierro, V.; Stein, N.; Boulanger, C.; Pizzi, A.; Celzard, A. Pore Structure and Electrochemical Performances of Tannin-Based Carbon Cryogels. *Biomass Bioenergy* **2012**, *39*, 274–282.
- (13) Li, X.; Basso, M. C.; Braghiroli, F. L.; Fierro, V.; Pizzi, A.; Celzard, A. Tailoring the Structure of Cellular Vitreous Carbon Foams. *Carbon* **2012**, *50*, 2026–2036.
- (14) Braghiroli, F. L.; Fierro, V.; Izquierdo, M. T.; Parmentier, J.; Pizzi, A.; Celzard, A. Nitrogen-Doped Carbon Materials Produced from Hydrothermally Treated Tannin. *Carbon* **2012**, *50*, 5411–5420.
- (15) Szczurek, A.; Fierro, V.; Pizzi, A.; Celzard, A. Mayonnaise, Whipped Cream and Meringue, a New Carbon Cuisine. *Carbon* **2013**, *58*, 245–248.
- (16) Celzard, A.; Fierro, V.; Pizzi, A.; Zhao, W. Multifunctional Porous Solids Serived from Tannins. *J. Phys. Conf. Series* **2013**, *416*, 012023.
- (17) Szczurek, A.; Fierro, V.; Pizzi, A.; Stauber, M.; Celzard, A. Carbon Meringues Derived from Flavonoid Tannins. *Carbon* **2013**, *65*, 214–227.
- (18) Szczurek, A.; Fierro, V.; Pizzi, A.; Celzard, A. Emulsion-Templated Porous Carbon Monoliths Derived from Tannins. *Carbon* **2014**, *74*, 352–362.
- (19) Szczurek, A.; Amaral-Labat, G.; Fierro, V.; Pizzi, A.; Celzard, A. Chemical Activation of Tannin-Based Hydrogels by Soaking in KOH and NaOH Solutions. *Microporous Mesoporous Mater.* **2014**, *196*, 8–17.
- (20) Jana, P.; Fierro, V.; Pizzi, A.; Celzard, A. Biomass-Derived, Thermally Conducting, Carbon Foams for Seasonal Thermal Storage. *Biomass Bioenergy* **2014**, *67*, 312–318.

- (21) Jenkins, G. M.; Kawamura, K.; Ban, L. L. Formation and Structure of Polymeric Carbons. *Proc. R. Soc. London, Ser. A* **1972**, 327, 501–517.
- (22) Odum, T. W.; Huang, J. L.; Kim, P.; Lieber, C. M. Atomic Structure and Electronic Properties of Single-Walled Carbon Nanotubes. *Nature* **1998**, 391, 62–64.
- (23) Kotakoski, J.; Krasheninnikov, A. V.; Kaiser, U.; Meyer, J. C. From Point Defects in Graphene to Two-Dimensional Amorphous Carbon. *Phys. Rev. Lett.* **2011**, 106, 105505.
- (24) Ferrari, A. C.; Kleinsorge, B.; Adamopoulos, G.; Robertson, J.; Milne, W. I.; Stolojan, V.; Brown, L. M.; LiBassi, A.; Tanner, B. K. Determination of Bonding in Amorphous Carbons by Electron Energy Loss Spectroscopy, Raman Scattering and X-Ray Reflectivity. *J. Non-Cryst. Solids* **2000**, 266, 765–768.
- (25) Haerle, R.; Riedo, E.; Pasquarello, A.; Baldereschi, A. p2/sp3 Hybridization Ratio in Amorphous Carbon from C1s Core-Level Shifts: X-Ray Photoelectron Spectroscopy and First-Principles Calculation. *Phys. Rev. B: Condens. Matter Mater. Phys.* **2001**, 65, 045101.
- (26) Ferrari, A. C. Determination of Bonding in Diamond-Like Carbon by Raman Spectroscopy. *Diamond Relat. Mater.* **2002**, 11, 1053–1061.
- (27) Pimenta, M. A.; Dresselhaus, G.; Dresselhaus, M. S.; Cancado, L. G.; Jorio, A.; Saito, R. Studying Disorder in Graphite-Based Systems by Raman Spectroscopy. *Phys. Chem. Chem. Phys.* **2007**, 9, 1276–1290.
- (28) Hawelek, L.; Brodka, A.; Dore, J. C.; Hannon, A. C.; Iijima, S.; Yudasaka, M.; Ohba, T.; Kaneko, K.; Burian, A. Structural Modeling of Dahlia-Type Single-Walled Carbon Nanohorn Aggregates by Molecular Dynamics. *J. Phys. Chem. A* **2013**, 117, 9057–9061.
- (29) Calo, J. M.; Hall, P. J. The Application of Small Angle Scattering Techniques to Porosity Characterization in Carbons. *Carbon* **2004**, 42, 1299–1304.
- (30) Hawelek, L.; Brodka, A.; Dore, J. C.; Honkimaki, V.; Burian, A. The Atomic Scale Structure of CXV Carbon: Wide-Angle X-ray Scattering and Modeling Studies. *J. Phys.: Condens. Matter* **2013**, 25, 454203.
- (31) Hawelek, L.; Kolano-Burian, A.; Szade, J.; Maziarz, W.; Woznica, N.; Burian, A. The Atomic Scale Structure of Nanographene Platelets Studied by X-Ray Diffraction, High-Resolution Transmission Electron Microscopy and Molecular Dynamics. *Diamond Relat. Mater.* **2013**, 35, 40–46.
- (32) O'Malley, B.; Snook, I.; McCulloch, D. Reverse Monte Carlo Analysis of the Structure of Glassy Carbon Using Electron-Microscopy Data. *Phys. Rev. B: Condens. Matter Mater. Phys.* **1998**, 57, 14148.
- (33) Lastoskie, C.; Gubbins, K. E.; Quirke, N. Pore Size Distribution Analysis of Microporous Carbons: a Density Functional Theory Approach. *J. Phys. Chem.* **1993**, 97, 4786–4796.
- (34) Braghioroli, F. L.; Fierro, V.; Izquierdo, M. T.; Parmentier, J.; Pizzi, A.; Celzard, A. Kinetics of the Hydrothermal Treatment of Tannin for Producing Carbonaceous Microspheres. *Bioresour. Technol.* **2014**, 151, 271–277.
- (35) Schlenz, H.; Neuefeind, J.; Rings, S. High-Energy X-Ray Diffraction Study of Amorphous ($\text{Si}_{0.71}\text{Ge}_{0.29}\text{O}_2$). *J. Phys.: Condens. Matter* **2003**, 15, 4919–4926.
- (36) Poulsen, H. F.; Neuefeind, J.; Neumann, H. B.; Schneider, J. R.; Zeidler, M. D. Amorphous Silica Studied by High Energy X-Ray Diffraction. *J. Non-Cryst. Solids* **1995**, 188, 63–74.
- (37) Hawelek, L.; Koloczek, J.; Burian, A.; Dore, J. C.; Honkimaki, V.; Kyotani, T. Application of Image Plate for Structural Studies of Carbon Nanotubes by High-Energy X-Ray Diffraction. *J. Alloys Compd.* **2005**, 401, 51–54.
- (38) Stewart, J. P. J. Optimization of Parameters for Semiempirical Methods VI: More Modifications to the NDDO Approximations and Re-Optimization of Parameters. *J. Mol. Model.* **2013**, 19, 1–32.
- (39) Mitchell, G. R. Eliminating the Small-Angle Component of the Scattering Calculated for Models. *Acta Crystallogr., Sect. A: Cryst. Phys., Diff., Theor. Gen. Crystallogr.* **1981**, 37, 488–2490.
- (40) Elliott, S. R. The Origin of the First Sharp Diffraction Peak in the Structure Factor of Covalent Glasses and Liquids. *J. Phys.: Condens. Matter* **1992**, 4, 7661–27678.
- (41) Elliott, S. R. Extended-Range Order, Interstitial Voids and the First Sharp Diffraction Peak of Network Glasses. *J. Non-Cryst. Solids* **1995**, 182, 40–248.
- (42) Warren, B. E. X-Ray Diffraction in Random Layer Lattices. *Phys. Rev.* **1941**, 59, 693–698.
- (43) Warren, B. E.; Bodenstein, P. The Diffraction Pattern of Fine Particle Carbon Blacks. *Acta Crystallogr.* **1965**, 18, 282–286.
- (44) Li, Z. Q.; Lu, C. J.; Xia, Z. P.; Zhou, Y.; Luo, Z. X-Ray Diffraction Patterns of Graphite and Turbostratic Carbon. *Carbon* **2007**, 45, 1686–1695.
- (45) Szczygalska, A.; Burian, A.; Dore, J. C. Paracrystalline Structure of Activated Carbons. *J. Phys.: Condens. Matter* **2001**, 13, 5545–5561.
- (46) Warren, B. E. *X-ray Diffraction*; Dover Publications, Inc.: New York, 2014.
- (47) Yang, D.; Velamakanni, A.; Bozkoklu, G.; Park, S.; Stoller, M.; Piner, R. D.; Stankovich, S.; Jung, I.; Field, D. A.; Ventrice, C. A., Jr.; et al. Chemical Analysis of Graphene Oxide Films after Heat and Chemical Treatments by X-Ray Photoelectron and Micro-Raman Spectroscopy. *Carbon* **2009**, 47, 145–152.
- (48) Datsyuk, V.; Kalyva, M.; Papagelis, K.; Parthenios, J.; Tasis, D.; Siokou, A.; Kallitsis, I.; Galotis, C. Chemical Oxidation of Multiwalled Carbon Nanotubes. *Carbon* **2008**, 46, 833–840.
- (49) Kim, S.; Zhou, S.; Hu, Y.; Acik, M.; Chabal, Y. J.; Berger, C.; Heer, W.; Bongiorno, A.; Riedo, E. Room-Temperature Metastability of Multilayer Graphene Oxide Films. *Nat. Mater.* **2012**, 11, 544–549.
- (50) Estrade-Szwarckopf, H. XPS Photoemission in Carbonaceous Materials: a “Defect” Peak beside the Graphitic Asymmetric Peak. *Carbon* **2004**, 42, 1713–1721.
- (51) Pasch, H.; Pizzi, A.; Rode, K. MALDI–TOF Mass Spectrometry of Polyflavonoid Tannins. *Polymer* **2001**, 42, 7531–7539.
- (52) Pizzi, A.; Tondi, G.; Pasch, H.; Celzard, A. Matrix-Assisted Laser Desorption/Ionization Time-of-Flight Structure Determination of Complex Thermoset Networks: Polyflavonoid Tannin–Furanic Rigid Foams. *J. Appl. Polym. Sci.* **2008**, 110, 1451–1456.
- (53) Kang, S.; Li, X.; Fan, J.; Chang, J. Characterization of Hydrochars Produced by Hydrothermal Carbonization of Lignin, Cellulose, D-Xylose, and Wood Meal. *Ind. Eng. Chem. Res.* **2012**, 51, 9023–9031.
- (54) Sevilla, M.; Fuertes, A. B. The Production of Carbon Materials by Hydrothermal Carbonization of Cellulose. *Carbon* **2009**, 47, 2281–2289.
- (55) Yao, C.; Shin, Y.; Wang, L.-Q.; Windisch, C. F.; Samuels, W. D.; Arey, B. W.; Wang, C.; Risen, W. M.; Exarhos, G. J. Hydrothermal Dehydration of Aqueous Fructose Solutions in a Closed System. *J. Phys. Chem. C* **2007**, 111, 15141–15145.
- (56) Hawelek, L.; Woznica, N.; Brodka, A.; Fierro, V.; Celzard, A.; Bulou, A.; Burian, A. Graphene-Like Structure of Activated Anthracites. *J. Phys.: Condens. Matter* **2012**, 24, 495303.
- (57) Pei, S.; Cheng, H. M. The Reduction of Graphene Oxide. *Carbon* **2012**, 50, 3210–3228.
- (58) Chiang, Y. C.; Lee, C. Y.; Lee, H. C. Surface Chemistry of Polyacrylonitrile- and Rayon-Based Activated Carbon Fibers after Post-Heat Treatment. *Mater. Chem. Phys.* **2007**, 101, 199–210.
- (59) Yamada, Y.; Yasuda, H.; Murota, K.; Nakamura, M.; Sodesawa, T.; Sato, S. Analysis of Heat-Treated Graphite Oxide by X-Ray Photoelectron Spectroscopy. *J. Mater. Sci.* **2013**, 48, 8171–8198.
- (60) Bagri, A.; Mattevi, C.; Acik, M.; Chabal, Y. J.; Chhowalla, M.; Shenoy, V. B. Structural Evolution during the Reduction of Chemically Derived Graphene Oxide. *Nat. Chem.* **2010**, 2, 581–587.
- (61) Ghaderi, N.; Peressi, M. First-Principle Study of Hydroxyl Functional Groups on Pristine, Defected Graphene, and Graphene Epoxide. *J. Phys. Chem. C* **2010**, 114, 21625–21630.
- (62) Qi, X.; Guo, X.; Zheng, C. Density Functional Study the Interaction of Oxygen Molecule with Defect Sites of Graphene. *Appl. Surf. Sci.* **2012**, 259, 195–200.

- (63) Kumar, V.; Bernardi, M.; Grossman, J. The Impact of Functionalization on the Stability, Work Function, and Photoluminescence of Reduced Graphene Oxide. *ACS Nano* **2013**, *7*, 1638–21645.
- (64) Gao, W.; Alemany, L. B.; Ci, L.; Ajayan, P. M. New Insights into the Structure and Reduction of Graphite Oxide. *Nat. Chem.* **2009**, *1*, 403–408.
- (65) Harris, P. J. F.; Liu, Z.; Suenaga, K. Imaging the Atomic Structure of Activated Carbon. *J. Phys.: Condens. Matter* **2008**, *20*, 362201.
- (66) Kotakoski, J.; Meyer, J. C.; Kurasch, S.; Santos-Cottin, D.; Kaiser, U.; Krashennnikov, A. V. Stone-Wales-Type Transformations in Carbon Nanostructures Driven by Electron Irradiation. *Phys. Rev. B: Condens. Matter Mater. Phys.* **2011**, *83*, 245420.
- (67) Ugeda, M. M.; Brihuega, I.; Hiebel, F.; Mallet, P.; Veuillen, J.-Y.; Gomez-Rodriguez, J. M.; Yndurain, F. Electronic and Structural Characterization of Divacancies in Irradiated Graphene. *Phys. Rev. B: Condens. Matter Mater. Phys.* **2012**, *85*, 121402.
- (68) Harris, P. J. F. Fullerene-Like Models for Microporous Carbon. *J. Mater. Sci.* **2013**, *48*, 565–577.
- (69) Bagri, A.; Grantab, R.; Medhekar, N. V.; Shenoy, V. B. Stability and Formation Mechanisms of Carbonyl- and Hydroxyl-Decorated Holes in Graphene Oxide. *J. Phys. Chem. C* **2010**, *114*, 12053–12061.